Search for Neutrinoless Double-Beta Decay with the Complete EXO-200 Dataset

G. Anton,[1] I. Badhrees,[2,a] P.S. Barbeau,[3] D. Beck,[4] V. Belov,[5] T. Bhatta,[6] M. Breidenbach,[7] T. Brunner,[8,9] G.F. Cao,[10] W.R. Cen,[10] C. Chambers,[11,b] B. Cleveland,[12,c] M. Coon,[4] A. Craycraft,[11] T. Daniels,[13] M. Danilov,[5,d] L. Darroch,[8] S.J. Daugherty,[14] J. Davis,[7] S. Delaquis,[7,e] A. Der Mesrobian-Kabakian,[12] R. DeVoe,[15] J. Dilling,[9] A. Dolgolenko,[5] M.J. Dolinski,[16] J. Echevers,[4] W. Fairbank Jr.,[11] D. Fairbank,[11] J. Farine,[12] S. Feyzbakhsh,[17] P. Fierlinger,[18] D. Fudenberg,[15] P. Gautam,[16] R. Gornea,[2,9] G. Gratta,[15] C. Hall,[19] E.V. Hansen,[16] J. Hoessl,[1] P. Hufschmidt,[1] M. Hughes,[20] A. Iverson,[11] A. Jamil,[21] C. Jessiman,[2] M.J. Jewell,[15] A. Johnson,[7] A. Karelin,[5] L.J. Kaufman,[7,f] T. Koffas,[2] R. Krücken,[9] A. Kuchenkov,[5] K.S. Kumar,[22,g] Y. Lan,[9] A. Larson,[6] B.G. Lenardo,[15] D.S. Leonard,[23] G.S. Li,[15,h] S. Li,[4] Z. Li,[21] C. Licciardi,[12] Y.H. Lin,[16] R. MacLellan,[6] T. McElroy,[8] T. Michel,[1] B. Mong,[7] D.C. Moore,[21] K. Murray,[8] O. Njoya,[22] O. Nusair,[20] A. Odian,[7] I. Ostrovskiy,[20] A. Piepke,[20] A. Pocar,[17] F. Retière,[9] A.L. Robinson,[12] P.C. Rowson,[7] D. Ruddell,[13] J. Runge,[3] S. Schmidt,[1] D. Sinclair,[2,9] A.K. Soma,[20] V. Stekhanov,[5] M. Tarka,[17] J. Todd,[11] T. Tolba,[10] T.I. Totev,[8] B. Veenstra,[2] V. Veeraraghavan,[20] P. Vogel,[24] J.-L. Vuilleumier,[25] M. Wagenpfeil,[1] J. Watkins,[2] M. Weber,[15] L.J. Wen,[10] U. Wichoski,[12] G. Wrede,[1] S.X. Wu,[15] Q. Xia,[21] D.R. Yahne,[11] L. Yang,[4] Y.-R. Yen,[16] O.Ya. Zeldovich,[5] and T. Ziegler[1]

(EXO-200 Collaboration)

[1] *Erlangen Centre for Astroparticle Physics (ECAP), Friedrich-Alexander-University Erlangen-Nürnberg, Erlangen 91058, Germany*
[2] *Physics Department, Carleton University, Ottawa, Ontario K1S 5B6, Canada*
[3] *Department of Physics, Duke University, and Triangle Universities Nuclear Laboratory (TUNL), Durham, North Carolina 27708, USA*
[4] *Physics Department, University of Illinois, Urbana-Champaign, Illinois 61801, USA*
[5] *Institute for Theoretical and Experimental Physics named by A.I. Alikhanov of National Research Centre "Kurchatov Institute", 117218, Moscow, Russia*
[6] *Department of Physics, University of South Dakota, Vermillion, South Dakota 57069, USA*
[7] *SLAC National Accelerator Laboratory, Menlo Park, California 94025, USA*
[8] *Physics Department, McGill University, Montreal, Quebec, Canada*
[9] *TRIUMF, Vancouver, British Columbia V6T 2A3, Canada*
[10] *Institute of High Energy Physics, Beijing, China*
[11] *Physics Department, Colorado State University, Fort Collins, Colorado 80523, USA*
[12] *Department of Physics, Laurentian University, Sudbury, Ontario P3E 2C6, Canada*
[13] *Department of Physics and Physical Oceanography, University of North Carolina at Wilmington, Wilmington, NC 28403, USA*
[14] *Physics Department and CEEM, Indiana University, Bloomington, Indiana 47405, USA*
[15] *Physics Department, Stanford University, Stanford, California 94305, USA*
[16] *Department of Physics, Drexel University, Philadelphia, Pennsylvania 19104, USA*
[17] *Amherst Center for Fundamental Interactions and Physics Department, University of Massachusetts, Amherst, MA 01003, USA*
[18] *Technische Universität München, Physikdepartment and Excellence Cluster Universe, Garching 80805, Germany*
[19] *Physics Department, University of Maryland, College Park, Maryland 20742, USA*
[20] *Department of Physics and Astronomy, University of Alabama, Tuscaloosa, Alabama 35487, USA*
[21] *Wright Laboratory, Department of Physics, Yale University, New Haven, Connecticut 06511, USA*
[22] *Department of Physics and Astronomy, Stony Brook University, SUNY, Stony Brook, New York 11794, USA*
[23] *IBS Center for Underground Physics, Daejeon 34126, Korea*
[24] *Kellogg Lab, Caltech, Pasadena, California 91125, USA*
[25] *LHEP, Albert Einstein Center, University of Bern, Bern, Switzerland*

(Dated: June 7, 2019)

A search for neutrinoless double-beta decay ($0\nu\beta\beta$) in ^{136}Xe is performed with the full EXO-200 dataset using a deep neural network to discriminate between $0\nu\beta\beta$ and background events. Relative to previous analyses, the signal detection efficiency has been raised from 80.8% to $96.4 \pm 3.0\%$ and the energy resolution of the detector at the Q-value of ^{136}Xe $0\nu\beta\beta$ has been improved from $\sigma/E = 1.23\%$ to $1.15 \pm 0.02\%$ with the upgraded detector. Accounting for the new data, the median 90% confidence level $0\nu\beta\beta$ half-life sensitivity for this analysis is $5.0 \cdot 10^{25}$ yr with a total ^{136}Xe exposure of 234.1 kg·yr. No statistically significant evidence for $0\nu\beta\beta$ is observed, leading to a lower limit on the $0\nu\beta\beta$ half-life of $3.5 \cdot 10^{25}$ yr at the 90% confidence level.

Double-beta decay is a second-order weak transition in which two neutrons simultaneously decay into two protons. While the mode with emission of two electrons and two antineutrinos ($2\nu\beta\beta$) has been observed in sev-

eral nuclides in which single-beta decay is suppressed [1], the hypothetical neutrinoless mode ($0\nu\beta\beta$) [2] is yet to be discovered. The search for $0\nu\beta\beta$ is recognized as the most sensitive probe for the Majorana nature of neutrinos [3]. Its observation would provide direct evidence for a beyond-the-Standard-Model process that violates lepton number conservation, as well as help constrain the absolute mass scale of neutrinos [4].

Recent experiments probing a number of nuclides [5–9] have set lower limits on the $0\nu\beta\beta$ half-life with sensitivities in the range $10^{25} - 10^{26}$ yr at 90% confidence level (CL). Exploiting the advantages of a liquid xenon (LXe) cylindrical time projection chamber (TPC) filled with LXe enriched to 80.6% in ^{136}Xe [10], EXO-200 [11] achieved a sensitivity of $3.7 \cdot 10^{25}$ yr with the most recent $0\nu\beta\beta$ search [5], while the most sensitive search to date for the same isotope reached $5.6 \cdot 10^{25}$ yr [6]. Here we report on a search with similar sensitivity to the previous best search.

In Dec. 2018, EXO-200 completed data taking with the upgraded detector ("Phase II", May 2016 to Dec. 2018), after collecting an exposure similar to that of its first run ("Phase I", Sept. 2011 to Feb. 2014). This letter reports a search for $0\nu\beta\beta$ using the full EXO-200 dataset, which after data quality cuts [10] totals 1181.3 d of livetime. This represents approximately a 25% increase in exposure relative to the previous search [5] that already included nearly half of the Phase II dataset. In addition to the new data acquired between Jun. 2017 and Oct. 2018, this search introduces several analysis developments to optimize the detector sensitivity to $0\nu\beta\beta$, including the incorporation of a deep neural network (DNN) to discriminate between background and signal events.

In the EXO-200 detector, a common cathode splits the LXe TPC into two drift regions, each with radius ∼18 cm and drift length ∼20 cm. The TPC is enclosed by a radiopure thin-walled copper vessel. The electric field in the drift regions was raised from 380 V/cm in Phase I to 567 V/cm in Phase II. The ionization produced from interactions in the LXe is read out after being drifted to crossed-wire planes at each anode, while the scintillation light produced at the interaction time is collected by arrays of large area avalanche photodiodes (LAAPDs) [12] located behind the wire planes.

The underground location of the experiment, the Waste Isolation Pilot Plant (WIPP) near Carlsbad New Mexico, provides an overburden of 1624^{+22}_{-21} meters of water equivalent [13]. In addition to several layers of passive shielding, including ∼50 cm of HFE-7000 cryofluid [14], 5.4 cm of copper and ∼25 cm of lead in all directions [11], an active muon veto system with scintillator panels on four sides allows prompt identification of $> 94\%$ of the cosmic ray muons passing through the TPC. This system is also used in this analysis to reject background events arising from cosmogenically produced ^{137}Xe, which primarily decays via β emission with a half-life of 3.82 min [5, 15].

Each TPC event is reconstructed by grouping charge and light signals into individual energy deposits. Ionization signals measured by two wire planes, an induction plane (V-wires) and a collection plane (U-wires), provide information about the coordinates x and y perpendicular to the drift field. The z position, along the drift direction, is obtained from the time delay between the prompt light and the delayed charge signals together with the measured electron drift velocity [16]. Events reconstructed with single and multiple energy deposit(s) are referred to as "single-site" (SS) and "multi-site" (MS). $0\nu\beta\beta$ events are predominantly SS whereas backgrounds are mostly MS. While the main procedures for spatial reconstruction are the same as in previous searches [5, 10, 17], the $0\nu\beta\beta$ detection efficiency has been raised to $97.8 \pm 3.0\%$ ($96.4 \pm 3.0\%$) in Phase I (Phase II) from $82.4 \pm 3.0\%$ ($80.8 \pm 2.9\%$) [5] by relaxing two selection criteria. First, the time required for events to be separated from all other reconstructed events has been reduced from > 1 s to > 0.1 s. This time cut is still at least two orders of magnitude longer than expected from typical time-correlated backgrounds seen in the detector [13, 18], while the $0\nu\beta\beta$ efficiency loss due to accidental coincidence is reduced from 7% to 0.5%. Second, the search presented here includes events containing deposits without a detected V-wire signal if these deposits contribute $< 40\%$ of the total event energy, which were removed in the previous analyses. Because of the higher energy threshold for signal detection on the V-wires (∼200 keV) versus the U-wires (∼90 keV), a significant number of events with small energy deposits are well-reconstructed by the U-wires but incompletely on the V-wires, resulting in events with full z reconstruction but incomplete xy reconstruction for smaller energy deposits. Relaxing this 3D-cut criterion only recovers MS events and retrieves almost all potential $0\nu\beta\beta$ events with incomplete xy reconstruction due to small, separated energy deposits from bremsstrahlung. While $0\nu\beta\beta$ primarily induces SS events, the smaller fraction of MS $0\nu\beta\beta$ events can be distinguished from the dominant γ backgrounds using a discriminator for MS events (described below), resulting in an enhancement in the $0\nu\beta\beta$ half-life sensitivity.

Events within the fiducial volume (FV) are required to lie within a hexagon in the xy plane with apothem of 162 mm. They are further required to be more than 10 mm away from the cylindrical PTFE reflector, as well as the cathode and the V-wire planes. This FV contains $3.31 \cdot 10^{26}$ atoms of ^{136}Xe, with an equivalent mass of 74.7 kg. While the incomplete xy-matched energy deposits may fall outside the FV, this effect is determined by detector simulations to have a negligible effect on the estimated detection efficiency due to the energy requirements imposed on these events. The ^{136}Xe exposure of the entire dataset after data quality cuts and accounting for livetime loss due to vetoing events coincident with the

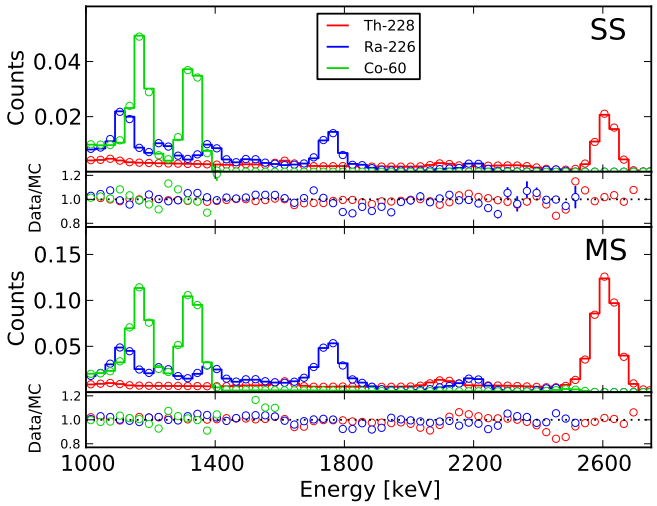

FIG. 1. (Color online) Comparison of energy distributions in data (circles) and MC (lines) for SS (top half) and MS (bottom half) events from calibration sources positioned near the cathode. The corresponding ratios between data and MC simulation are also shown.

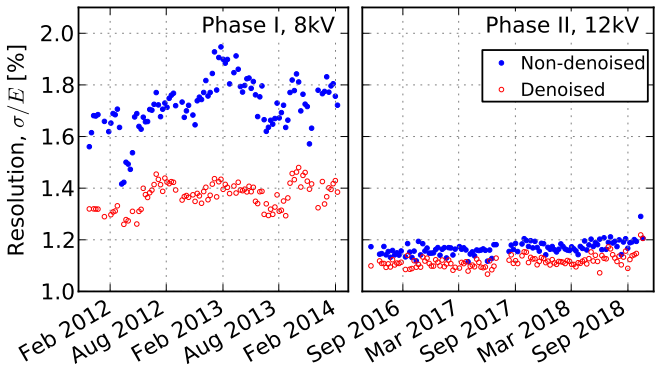

FIG. 2. (Color online) Energy resolution, σ/E, of SS events measured using a ^{228}Th calibration source deployed to a position near the cathode. The effect of the de-noising algorithm and weekly variation of the resolution at the 2615 keV ^{208}Tl γ line are shown for both Phase I and Phase II. The resolution worsened slightly after a xenon recovery in July 2017 due to a power outage. A degraded resolution due to an increase of excess noise is visible in last weeks of Phase II.

muon veto is 234.1 kg·yr, or 1727.5 mol·yr, with 117.4 (116.7) kg·yr in Phase I (Phase II).

The detector response to $0\nu\beta\beta$ decays and background interactions is modeled by a detailed Monte Carlo (MC) simulation based on GEANT4 [19]. This MC simulation models the energy deposits produced by interactions in the LXe, then propagates the ionization through the detector to produce waveforms associated to readout channels. These simulated waveforms are input to the same reconstruction and analysis framework used for data waveforms. Calibration data with external γ sources located 9 (11) cm away from the FV at set positions around the cathode (behind the anodes) [10] were regularly taken to validate the analysis.

After the previous EXO-200 $0\nu\beta\beta$ search [5], a small fraction of the observed candidate events presented light-to-charge ratios that were not fully consistent with their expected distributions. Using calibration and $2\nu\beta\beta$ data, the distribution of the light-to-charge ratio is measured and found to be approximately gaussian around the mean ratio. While keeping the maximal search sensitivity, a cut is imposed requiring that events are within 2.5σ of the mean of the distribution. This improves the previous cut [10], primarily aimed at removing α decays, by also removing poorly reconstructed β and γ events with an anomalous light-to-charge ratio. All systematic errors associated with the signal detection efficiency are summarized in Tab. I.

The reconstructed energy is determined by combining the anti-correlated charge and light signals [20] to optimize the resolution at the $0\nu\beta\beta$ decay energy of $Q_{\beta\beta} = 2457.83 \pm 0.37$ keV [21]. An offline de-noising algorithm [22], previously introduced to account for excess APD read-out noise observed in Phase I, has been further optimized with measurements of the light response of the detector and adapted for Phase II data. In addition, a proper modeling of mixed signals from the induced and collected charge in wires is introduced to the signal finder in the event reconstruction process. The resulting energy measurement shows good spectral agreement between data and simulation for SS and MS events using ^{228}Th, ^{226}Ra and ^{60}Co calibration sources as shown in Figure 1. The electronics upgrade carried out before Phase II data taking resulted in substantially improved resolution and stability, as illustrated in Figure 2. The calibration data shown is the ^{228}Th source regularly deployed to monitor the detector performance. The average detector resolution is determined by uniformly weighting all calibration data from several positions and accounting for the detector livetime. The averages for Phase I and Phase II are $\sigma/E\,(Q_{\beta\beta}) = 1.35 \pm 0.09\%$ and $1.15 \pm 0.02\%$, respectively.

All data, including those previously reported, were blinded to hide all candidate $0\nu\beta\beta$ SS events having energy within $Q_{\beta\beta} \pm 2\sigma$. No information about such events is used in the development of the techniques for this analysis. New background discriminators are studied to optimize the sensitivity of this search, while minimizing the systematic errors. The search for $0\nu\beta\beta$ is performed with a simultaneous maximum-likelihood (ML) fit to the SS and MS energy spectra, with the discriminators added as additional fit dimensions. While Phase I and Phase II are fit independently and then combined by summing their individual profile likelihoods for various signal hypotheses, both use the same background model developed in [18] composed of decays originating in the detector and surrounding materials. Systematic errors are included in the ML fit as nuisance parameters constrained

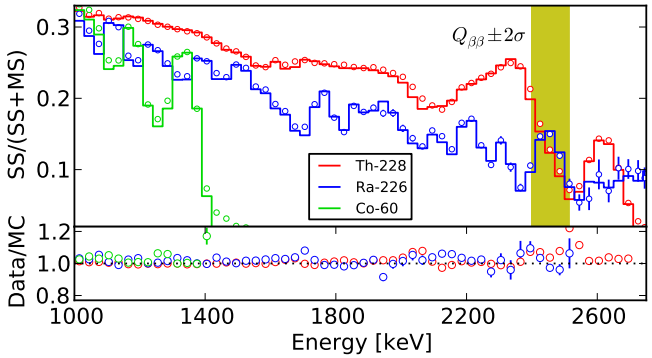

FIG. 3. (Color online) SS fractions, SS/(SS+MS), for MC (lines) and calibration data (circles) in Phase II using ^{60}Co (green), ^{226}Ra (blue) and ^{228}Th (red) sources positioned near the cathode. The bottom panel shows the ratio between data and MC simulation.

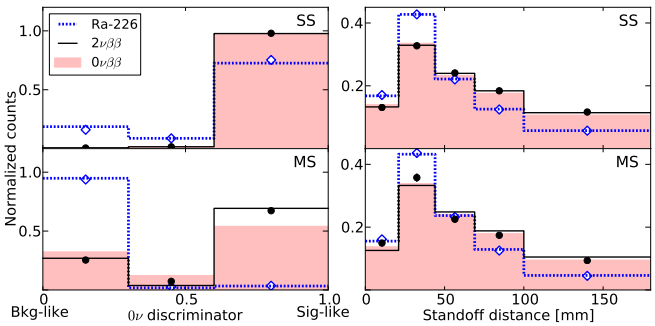

FIG. 4. (Color online) Comparison between data (dots) and MC (solid/dashed lines) for the DNN $0\nu\beta\beta$ discriminator (left) and standoff distance (right). Shown are the distributions from the ^{226}Ra calibration source (blue) and the background-subtracted $2\nu\beta\beta$ spectrum from low background data (black). The simulated distributions for $0\nu\beta\beta$ events are indicated by the red filled region. The difference in DNN distribution between $0\nu\beta\beta$ and $2\nu\beta\beta$ events in MS is due to the higher rate of bremsstrahlung at higher electron energy.

by normal distributions. The median 90% CL sensitivity is estimated using toy datasets (simulated trial experiments) generated from the MC probability density functions (PDFs) of the background model.

The primary topological discrimination of backgrounds is the SS/MS event classification. Figure 3 shows the agreement between source calibration data and MC for the "SS fraction," SS/(SS+MS). Because the relaxed 3D-cut recovers MS events, the SS fraction near $Q_{\beta\beta}$ is lowered from 24% (23%) to 12% (14%) for the ^{228}Th (^{226}Ra) source compared to previous searches. Systematic errors related to the SS fractions are determined by comparisons between data and MC. Taking into account different calibration sources at various positions, these systematics are evaluated to be 5.8% (4.6%) for Phase I (Phase II).

Additional event information can be used to further constrain backgrounds. In [17] the minimum distance between the event position and the closest material surface excluding the cathode, referred to as the "standoff distance," was introduced to constrain backgrounds originating from γ sources external to the LXe. Motivated by the results in [23], this analysis introduces a new discriminator for SS and MS events using a DNN that relies on the waveforms of U-wire signals and is found to outperform the searches in [5, 17]. The training inputs for the DNN are greyscale images built by arranging neighboring channels next to each other and encoding the amplitudes of U-wire waveforms as pixel values. The training data is produced in MC simulation for two classes of events: background-like, composed of γ events with uniform energy distribution between 1000 keV and 3000 keV; and signal-like $0\nu\beta\beta$ events with a random decay energy restricted to the same energy limits. The location of the simulated interactions of both types are drawn uniformly in the detector volume to focus discrimination only on the topological event characteristics. This MC dataset is populated with 50% of each class. It is divided into 90% for training and 10% for validation. The DNN architecture is inspired by the Inception architecture proposed by Google [24] and implemented with the Keras library [25] using the Tensorflow backend [26].

The agreement for the DNN discriminator between data and MC is improved when signals from U-wire waveforms are first identified by the signal finder in the EXO-200 reconstruction framework, and then used to regenerate the images. Since there is no spatial dependence in training the DNN for signal- and background-like events, the standoff distance is incorporated in the search as a third fit dimension for both SS and MS events. Figure 4 shows a comparison of these two discriminators between simulated and observed data distributions for the ^{226}Ra calibration source, and for the measured background-subtracted $2\nu\beta\beta$ distribution. While keeping as much discriminating power as possible, the binning used for each variable is selected to minimize systematic errors arising from imperfections in the MC simulation.

Since the fit cannot resolve the detailed location of backgrounds arising from materials far from the LXe vessel, the ^{238}U, ^{232}Th and ^{60}Co contributions from such components are alternated from their assumed locations. The resulting change in the expected number of events near $Q_{\beta\beta}$ is taken as the systematic error of the background model. This is evaluated to be 4.0% (4.6%) in Phase I (Phase II). In addition, toy studies were used to find the average bias in the expected number of events near $Q_{\beta\beta}$ arising from the measured spectral differences between data and MC for energy, DNN $0\nu\beta\beta$ discriminator and standoff distance. The differences between data and MC for their distributions obtained with the γ calibration sources are used to correct the predicted PDFs, while differences in the background-subtracted $2\nu\beta\beta$ distribution are used for β-like components. The relative differences between results with toy datasets generated

from the corrected PDFs, but fit without this correction, are added in quadrature for all contributors and sum to 5.8% (4.4%) in Phase I (Phase II). Tab. I summarizes the contributions to background errors, including other sources unchanged from previous searches.

TABLE I. Summary of systematic error contributions.

Source	Phase I	Phase II
Background errors		
Spectral shape agreement	5.8%	4.4%
Background model	4.0%	4.6%
Other [5]	1.5%	1.2%
Total error	7.1%	6.5%
Signal detection efficiency		
Fiducial volume	2.8%	2.6%
Partial 3D cut	$< 0.4\%$	$< 0.4\%$
Light-to-charge ratio	0.9%	0.9%
De-noising mis-rec	-	1.0%
Other [10]	$< 1.0\%$	$< 1.0\%$
Total error	3.1%	3.1%

The measured rate of radon decays in the LXe is used to constrain the appropriate background components arising from these atoms, as described in [10]. The relative rate of cosmogenically produced backgrounds is also constrained [13]. In addition, a possible difference between the energy scale from γ calibration sources (E_γ) and from single- or double-beta decays (E_β) is accounted for by a factor (B) that scales the energy of the β-like components in the ML fit, $E_\beta = BE_\gamma$. B is allowed to freely float and found to be consistent with unity to the subpercent level in both phases.

The 90% CL median sensitivity for this $0\nu\beta\beta$ search with the DNN $0\nu\beta\beta$ discriminator is evaluated to be $5.0 \cdot 10^{25}$ yr. The coverage is validated with toy MC studies and found to agree with Wilks's theorem [27, 28]. A secondary analysis is performed using a boosted decision trees (BDT) discriminator for MS events and the BDT discriminator designed in [5] for SS events as the second fit dimension. The BDT for MS is built on variables containing information on the energy fraction of the most energetic deposit, the spatial spread among deposits and the number of deposits. The BDT analysis provides comparable but slightly worse ($\sim$3%) sensitivity, suggesting that the discrimination power of the DNN discriminator can be mostly accounted for by careful construction of BDT variables. The DNN analysis was selected as the primary analysis prior to unblinding since it had the best sensitivity.

After unblinding the dataset, the SS candidate events within $Q_{\beta\beta} \pm 2\sigma$ were examined, which led us to find one event, originally with energy in this region, was misreconstructed by the de-noising algorithm. Its impact on the $0\nu\beta\beta$ detection efficiency is investigated, and found to only affect Phase II with an efficiency loss $< 1.0\%$. A conservative 1.0% error is also added to the signal detection efficiency.

ML fits are performed to Phase I and Phase II separately, and the best-fit results are shown in Figure 5. No statistically significant evidence for $0\nu\beta\beta$ is observed. The best-fit background contributions to $Q_{\beta\beta} \pm 2\sigma$ are shown in Tab. II. The rate normalized over the total fiducial Xe mass, including all isotopes, is $(1.7 \pm 0.2) \cdot 10^{-3}$ kg^{-1}yr^{-1}keV^{-1} and $(1.9 \pm 0.2) \cdot 10^{-3}$ kg^{-1}yr^{-1}keV^{-1} for Phase I and Phase II respectively. The lower limit on the ^{136}Xe $0\nu\beta\beta$ half-life is derived by profiling over all nuisance parameters, and results in $T_{1/2} > 1.7{\cdot}10^{25}$ yr ($T_{1/2} > 4.3{\cdot}10^{25}$ yr) at 90% CL in Phase I (Phase II), while the combined limit is $T_{1/2} > 3.5 \cdot 10^{25}$ yr. This corresponds to an upper limit on the Majorana neutrino mass of $\langle m_{\beta\beta} \rangle < (93 - 286)$ meV [3], using the nuclear matrix elements of [29–33] and phase space factor from [34].

TABLE II. Best-fit background contributions to $Q_{\beta\beta} \pm 2\sigma$ versus observed number of events in data.

(counts)	^{238}U	^{232}Th	^{137}Xe	Total	Data
Phase I	12.6	10.0	8.7	32.3±2.3	39
Phase II	12.0	8.2	9.3	30.9±2.4	26

EXO-200 has concluded its operations reaching a sensitivity to Majorana neutrino mass of $78 - 239$ meV, similar to the most sensitive searches for $0\nu\beta\beta$ to date [6–9]. The analysis presented here utilizes detailed event topology information, leading to a $\sim$25% improvement relative to the sensitivity using only event energy and simple SS/MS discriminators. This performance results from the unique capabilities of a monolithic LXe TPC, which includes good energy resolution, near maximal signal detection efficiency and strong topological discrimination of backgrounds. This combination holds promise for nEXO [35, 36], the planned tonne-scale successor to EXO-200, designed to achieve a sensitivity to $0\nu\beta\beta$ half-life of $\sim 10^{28}$ yr in ^{136}Xe.

EXO-200 is supported by DOE and NSF in the United States, NSERC in Canada, SNF in Switzerland, IBS in Korea, RFBR (18-02-00550) in Russia, DFG in Germany, and CAS and ISTCP in China. EXO-200 data analysis and simulation uses resources of the National Energy Research Scientific Computing Center (NERSC). We gratefully acknowledge the KARMEN collaboration for supplying the cosmic-ray veto detectors, and the WIPP for their hospitality.

[a] Permanent position with King Abdulaziz City for Science and Technology, Riyadh, Saudi Arabia
[b] Physics Department, McGill University, Montreal, Quebec, Canada
[c] Also at SNOLAB, Sudbury, ON, Canada

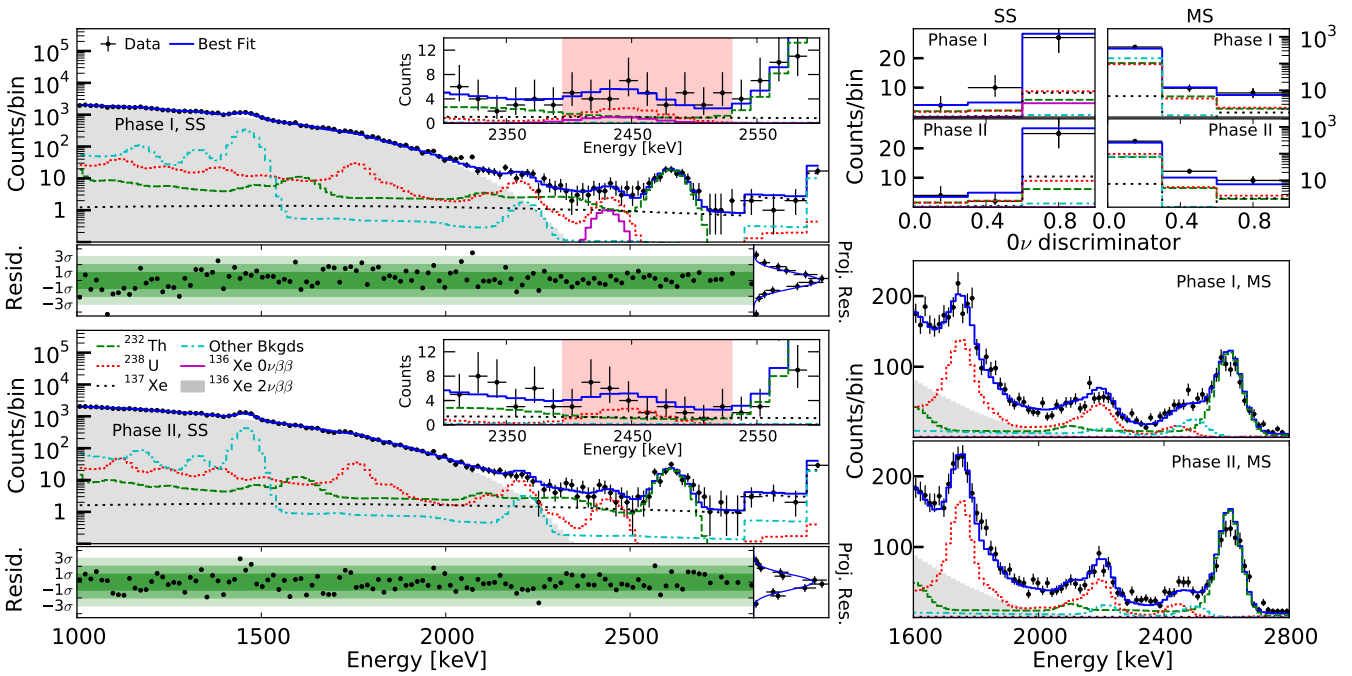

FIG. 5. (Color online) Best fit to the low background data SS energy spectrum for Phase I (top left) and Phase II (bottom left). The energy bins are 15 keV and 30 keV below and above 2800 keV, respectively. The inset shows a zoomed in view around the best-fit value for $Q_{\beta\beta}$. (top right) Projection of events in the range 2395 keV to 2530 keV on the DNN fit dimension for SS and MS events. (bottom right) MS energy spectra. The best-fit residuals typically follow normal distributions, with small deviations taken into account in the spectral shape systematic errors.

[d] Now at P.N.Lebedev Physical Institute of the Russian Academy of Sciences, Moscow, Russia
[e] Deceased
[f] Also at Physics Department and CEEM, Indiana University, Bloomington, IN, USA
[g] Now at Physics Department, University of Massachusetts, Amherst, MA, USA
[h] Corresponding author: ligs@stanford.edu

[1] M. Tanabashi *et al.* (Particle Data Group), Phys. Rev. D **98**, 030001 (2018).
[2] W. H. Furry, Phys. Rev. **56**, 1184 (1939).
[3] S. Dell'Oro, S. Marcocci, M. Viel, and F. Vissani, Adv. High Energy Phys. **2016**, 2162659 (2016), arXiv:1601.07512 [hep-ph].
[4] J. Engel and J. Menéndez, Rept. Prog. Phys. **80**, 046301 (2017), arXiv:1610.06548 [nucl-th].
[5] J. B. Albert *et al.* (EXO-200 Collaboration), Phys. Rev. Lett. **120**, 072701 (2018), arXiv:1707.08707 [hep-ex].
[6] A. Gando *et al.* (KamLAND-Zen Collaboration), Phys. Rev. Lett. **117**, 082503 (2016), [Addendum: Phys. Rev. Lett. **117**, 109903(2016)], arXiv:1605.02889 [hep-ex].
[7] C. Aalseth *et al.* (MAJORANA Collaboration), Phys. Rev. Lett. **120**, 132502 (2018), arXiv:1710.11608 [nucl-ex].
[8] M. Agostini *et al.* (GERDA Collaboration), Phys. Rev. Lett. **120**, 132503 (2018), arXiv:1803.11100 [nucl-ex].
[9] C. Alduino *et al.* (CUORE), Phys. Rev. Lett. **120**, 132501 (2018), arXiv:1710.07988 [nucl-ex].
[10] J. B. Albert *et al.* (EXO-200 Collaboration), Phys. Rev. C **89**, 015502 (2014).
[11] M. Auger *et al.*, JINST **7**, P05010 (2012), arXiv:1202.2192 [physics.ins-det].
[12] R. Neilson *et al.*, Nucl. Inst. & Meth. A **608**, 68 (2009), arXiv:0906.2499 [physics.ins-det].
[13] J. B. Albert *et al.* (EXO-200 Collaboration), JCAP **1604**, 029 (2016), arXiv:1512.06835 [nucl-ex].
[14] 3M HFE-7000, http://www.3m.com,.
[15] G. C. Carlson, W. C. Schick, W. L. Talbert, and F. K. Wohn, Nucl. Phys. **A125**, 267 (1969).
[16] J. B. Albert *et al.* (EXO-200 Collaboration), Phys. Rev. **C95**, 025502 (2017), arXiv:1609.04467 [physics.ins-det].
[17] J. B. Albert *et al.* (EXO-200 Collaboration), Nature **510**, 229 (2014), arXiv:1402.6956 [nucl-ex].
[18] J. B. Albert *et al.* (EXO-200 Collaboration), Phys. Rev. C **92**, 015503 (2015).
[19] J. Allison *et al.*, IEEE Trans. Nucl. Sci. **53**, 270 (2006).
[20] E. Conti *et al.*, Phys. Rev. B **68**, 054201 (2003).
[21] M. Redshaw, E. Wingfield, J. McDaniel, and E. G. Myers, Phys. Rev. Lett. **98**, 053003 (2007).
[22] C. G. Davis *et al.* (EXO-200 Collaboration), JINST **11**, P07015 (2016), arXiv:1605.06552 [physics.ins-det].
[23] S. Delaquis *et al.* (EXO-200 Collaboration), JINST **13**, P08023 (2018), arXiv:1804.09641 [physics.ins-det].
[24] C. Szegedy *et al.*, CoRR **abs/1409.4842** (2014), arXiv:1409.4842.
[25] F. Chollet *et al.*, "Keras," `https://keras.io` (2015).
[26] M. Abadi *et al.*, "TensorFlow: Large-scale machine learning on heterogeneous systems," (2015), software available from tensorflow.org.
[27] S. S. Wilks, Ann. Math. Statist. **9**, 60 (1938).
[28] G. Cowan, *Statistical Data Analysis*, Oxford science publications (Clarendon Press, 1998).

[29] J. Barea, J. Kotila, and F. Iachello, Phys. Rev. C **91**, 034304 (2015).
[30] N. L. Vaquero, T. R. Rodríguez, and J. L. Egido, Phys. Rev. Lett. **111**, 142501 (2013).
[31] J. Engel, F. Šimkovic, and P. Vogel, Phys. Rev. C **89**, 064308 (2014).
[32] J. Menéndez, A. Poves, E. Caurier, and F. Nowacki, Nucl. Phys. A **818**, 139 (2009).
[33] M. T. Mustonen and J. Engel, Phys. Rev. C **87**, 064302 (2013).
[34] J. Kotila and F. Iachello, Phys. Rev. C **85**, 034316 (2012), arXiv:1209.5722 [nucl-th].
[35] S. Al Kharusi *et al.*, pre-print (2018), arXiv:1805.11142 [physics.ins-det].
[36] J. B. Albert *et al.* (nEXO), Phys. Rev. **C97**, 065503 (2018), arXiv:1710.05075 [nucl-ex].